THE INTERCALIBRATION OF SOHO/EIT, CDS-NIS, AND TRACE

David H. Brooks [1] and Harry P. Warren
E. O. Hulburt Center for Space Research, Code 7670, Naval Research Laboratory, Washington, DC 20375
dhbrooks@ssd5.nrl.navy.mil,hwarren@nrl.navy.mil

ABSTRACT

Using coordinated observations of a quiet coronal region, we study the intercalibration of the CDS and EIT instruments on board the *Solar and Heliospheric Observatory (SOHO)* and the *Transition Region and Coronal Explorer (TRACE)*. We derive the Differential Emission Measure (DEM) distribution from CDS spectral line intensities, and convolve it with updated EIT and TRACE temperature response functions, calculated with the latest atomic data from the CHIANTI database, to predict count rates in their observing channels. We examine different analysis methods, and briefly discuss some more advanced aspects of atomic modeling such as the density dependence of the ionization fractions. We investigate the implications for our study using data from the ADAS database. We find that our CDS DEM can predict the TRACE and EIT 171 Å and 195 Å channel count rates to within 25%. However, the accuracy of the predictions depends on the ionization fractions and elemental abundances used. The TRACE 284 Å and EIT 284 Å and 304 Å filter predictions do not agree well with the observations, even after taking the contribution from the optically thick He II 304 Å line into account. The different CDS DEM solutions we derive using different ionization fractions produce fairly similar results: most of the CDS line intensities are reproduced to within 20% with only around one fifth reproduced to worse than 50%. However, the comparison provides us with further clues with which to explain the discrepancies found for some lines, and highlights the need for accurate equilibrium ionization balance calculations even at low density.

Subject headings: Sun: UV radiation—Sun: corona—Techniques: spectroscopic

1. Introduction

The SOlar and Heliospheric Observatory (SOHO, Domingo et al. 1995) was launched in 1995 and for nearly a decade has provided a wealth of scientific observations. Together with the Transition Region and Coronal Explorer (TRACE, Handy et al. 1999) the dynamic nature of the solar upper atmosphere has been revealed. EUV coordinated spectroscopic and imaging observations have been used to attack the outstanding problems in solar physics, and atomic databases and analysis methods have been developed in support of future instrumentation that have been tested in the study of SOHO and TRACE data.

However, fundamental to the understanding of such multi-instrument datasets is our confidence in the cross-calibration of the line intensities from the SOHO spectrometers, and count rates from the SOHO and TRACE imagers. Uncertainties in intensity calibration affect our ability to accurately derive plasma properties such as electron density, temperature, or elemental abundances, which are important for comparison with, or entry into, physical models. Furthermore, differences in spectral reduction procedures for several of the more complicated instruments, for example, the Coronal Diagnostic Spectrometer (CDS, Harrison et al. 1995), affect intensity measurements, and it is desirable to quantify these differences to ensure they have no major influence on the cross-comparison of different instruments. This is one of the subjects of the present paper.

In addition, despite efforts prior to SOHO to benchmark atomic data for the developing mission (Lang 1994), and possibly standardize widely used spectroscopic analysis methods such as Differential Emission Measure (DEM, Harrison & Thompson 1991), there remains no universally accepted DEM or atomic modeling strategy to take us through the analysis pathway from obtaining spectral line intensities to delivery of the plasma temperature structure. The DEM method also continues to be a subject of criticism, but one of its most useful applications is intensity prediction for internal spectrometer and cross-instrument *in-flight* calibration checks.

Finally, when analyzing TRACE or SOHO-EIT (Extreme ultraviolet Imaging Telescope, Delaboudiniere et al. 1995) images, use is often made of archived standard temperature response functions. However, when cross-analysis is made with observations by different instruments such as CDS, there are often inconsistencies in the atomic data adopted. For example, even if the atomic database used is the same, the response functions in the standard archives may be calculated at a fixed density which may not be applicable to the specific CDS observations analyzed. The same is true when comparing to e.g. 1-D hydrodynamic models, which may contain a radiative loss curve calculated with different ionization fractions or even abundances.

It is the objective of this work to tackle these issues by examining different data reduction procedures, DEM methods, and atomic databases, and studying the consistency between intensity measurements from the EIT and TRACE images and CDS-Normal Incidence Spectrometer (NIS) spectral line intensities. Therefore, we study a set of coordinated SOHO/EIT, CDS, and TRACE intercalibration observations taken on 1998 May 1. In doing this analysis we take care to ensure that consistency is obtained in all the atomic data that goes into the full cycle of analysis. Thus the same ionization fractions, elemental abundances, collisional excitation rates etc. are used for calculating response functions, DEM, synthetic spectra, radiated power loss curves etc. We then briefly discuss some of the more advanced atomic models currently being developed, and examine the consequences of introducing approximate representations of such models.

The outline of the paper is as follows. In §2 we describe the observations and the instrument programs run. We also discuss the coalignment of the data from the three instruments. In §3

[1] George Mason University, 4400 University Drive, Fairfax, VA 22020

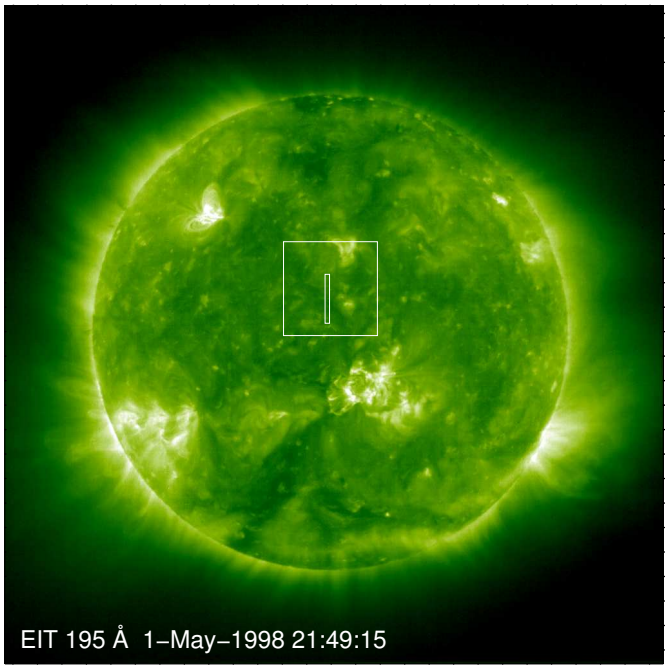

Fig. 1.— A full-disk EIT 195 Å image showing the CDS and TRACE fields of view.

we describe the atomic data used. In §4 we discuss the CDS data reduction procedures and spectral line fitting method used. We then describe the DEM method adopted and derive the electron pressure of the observed region using diagnostic line ratios. This value is used for calculating the contribution functions necessary for the DEM analysis. We also discuss our reasons for eliminating some lines from the analysis, the DEM distribution itself, and the discrepancies found between observed and theoretical line intensities. In §5 we describe the TRACE data reduction procedures applied and calculate new temperature response functions for the observing channels. The results are compared to the previously archived functions. §6 follows the same outline as for §5 but for EIT. In §7 we convolve the DEM solution with the relevant response functions to predict the EIT and TRACE filter channel count rates. In §8 we give a brief discussion of atomic physics issues and re-derive the DEM solution using different ionization fraction datasets. The consequences for the solution, the discrepant line intensities, and the predicted TRACE and EIT count rates are discussed. In §9 we discuss the application of our results to hydrodynamic models, and in §10 we summarize our conclusions.

2. Observations and Coalignment

SOHO/EIT, CDS/NIS, and TRACE made coordinated observations of a region of quiet Sun on 1998 May 1. Figure 1 shows an EIT 195 Å full disk image taken at 21:49:15UT with the TRACE and CDS/NIS fields of view (FOV) overlaid at their pointing locations. The TRACE FOV was $512'' \times 512''$ and the CDS FOV was $20'' \times 240''$.

CDS ran several observing programs between 12:56 and 23:20UT, but in this paper we only analyze data taken between 22:21:54 and 23:19:24UT. During this time the CDS/NIS observing sequence used was NISAT_S (ID 17 var.2) which takes full spectra in both the NIS channels from 308–381 Å and 513–633 Å. The $2'' \times 240''$ slit was used for the best spectral resolution. CDS rastered over 10 pointing positions to complete the FOV.

EIT also ran several observing sequences during this time period and mainly performed cross-calibration activities using 195 Å full disk observations as shown in the figure. Several of these images were obtained during the NISAT_S observations and we used these for analysis. Cross-calibration images in the 171 Å and 284 Å channels were taken around 20:00 to 20:20UT, and we also used these in our study. TRACE made observations in multiple channels throughout the time period of the NISAT_S observations and we selected 171 Å, 195 Å, and 284 Å images taken around 21:45 to 21:48UT for analysis.

The EIT and TRACE images and CDS rasters were coaligned and Figures 2 and 3 show example images and intensity plots to demonstrate the accuracy of the procedures. Coaligned TRACE and EIT 171 Å images are shown at 21:48:05UT and 20:01:10UT. Coaligned 195 Å images are shown at 21:49:05UT and 21:49:15UT. Coaligned 284 Å images are shown at 21:45:58UT and 20:06:58UT. The CDS FOV is rotated to the image time and overlaid at each time on the images. Note the large time delay between the EIT and TRACE images for the 171 and 284 Å channels. We verified that the TRACE data varied by less than $\sim 5\%$ during the time between the TRACE and EIT images in the figure. This was done by measuring the average intensity per full resolution pixel over the CDS FOV in series of TRACE images taken between the times of the TRACE and EIT images. TRACE images were taken approximately every 10-12 min with a gap of around 30 min between 20:56 and 20:26UT.

The visible structure in the images looks qualitatively similar, though the He II 304 Å network emission is more pronounced in the TRACE 284 Å image than in the EIT one. Figure 3 shows plots of the intensity as a function of solar y position along the CDS slit for the EIT images. Representative spectral lines were chosen from CDS to show the intensity variation observed by it at the approximate formation temperatures of the main contributing lines to the EIT channels. These are overplotted as dashed lines in the figure. The differences between the normalized intensities are generally small for the 171 Å and 195 Å channels, with a maximum of about 25%. The variations are larger for the 284 Å channel, reflecting the difficulty in finding a good CDS proxy line for the combination of emission from He II and other lines emitting around $\log T_e = 5.8$ in this pass-band.

3. Atomic Data

The fundamental and derived atomic data used in this work come from the CHIANTI version 4.2 (Dere et al. 1997; Young et al. 2003) and ADAS (Atomic Data and Analysis Structure, Summers 2001) version 2.9 databases. The electron collisional excitation, deexcitation, and spontaneous radiative decay rates are generally taken from the latest calculations in both cases. Details can be found in the respective databases.

One of our objectives in this analysis was to assess the effects of different ionization balance calculations on our results. In particular, we were interested in the role of metastable states and the effects of finite plasma electron density. Therefore, we used several sources for the ion fractional abundances. From the CHIANTI database we used the zero density results of Mazzotta et al. (1998). From the ADAS database we used the zero density results of Arnaud & Rothenflug (1985) (and Arnaud & Raymond 1992, for Fe) scaled for electron density effects following the methods of Summers (1974). A further discussion of relevant

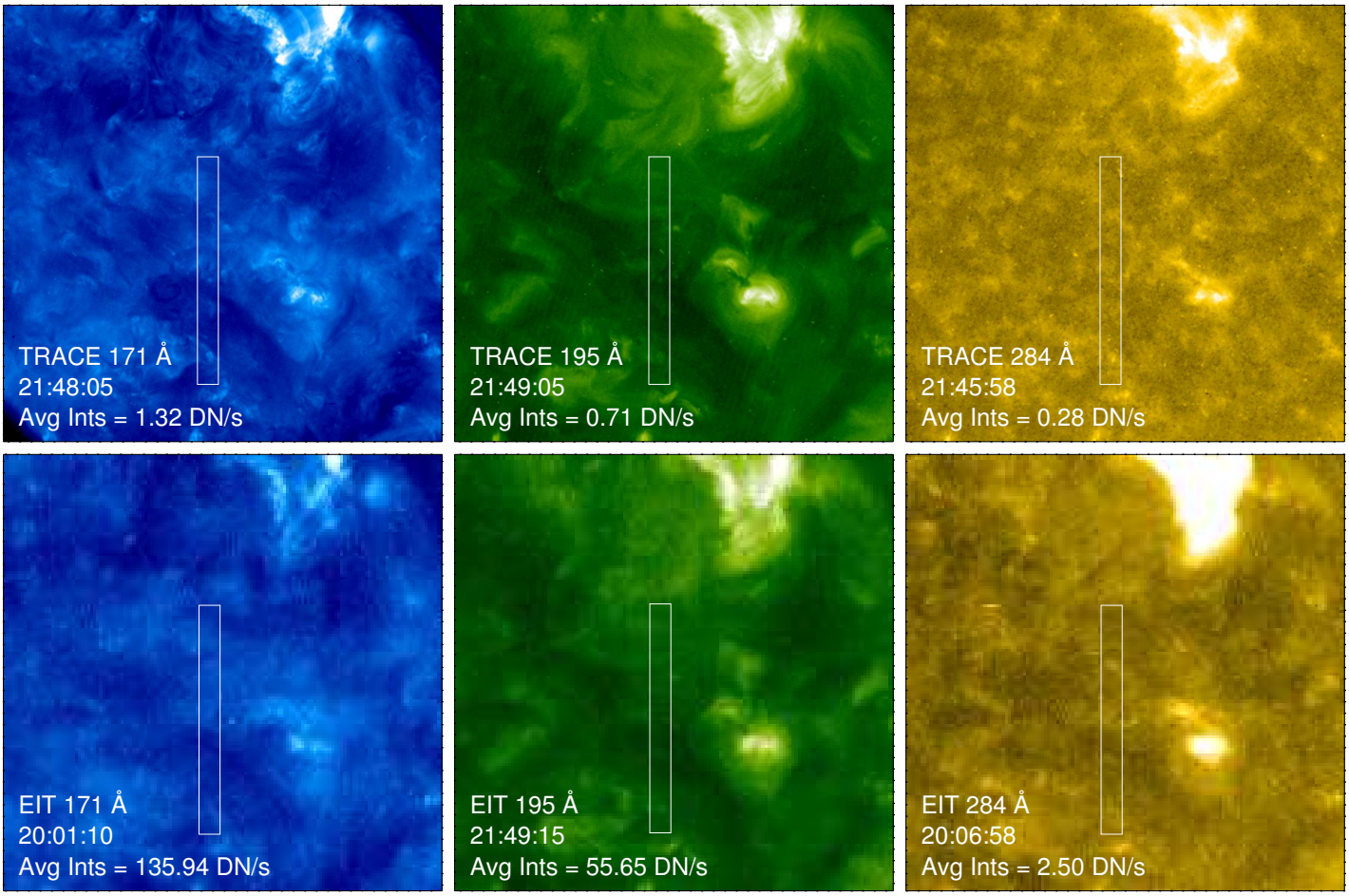

Fig. 2.— TRACE and EIT images from the intercalibration observations. The EIT images are normalized so that they have the same intensity as the corresponding TRACE image. Both the TRACE and EIT images are scaled logarithmically. Note that there is a significant time delay between the EIT and TRACE images for the 171 Å and 284 Å channels. The CDS field of view is shown. The average TRACE or EIT intensity per full resolution pixel in the CDS field of view is also indicated.

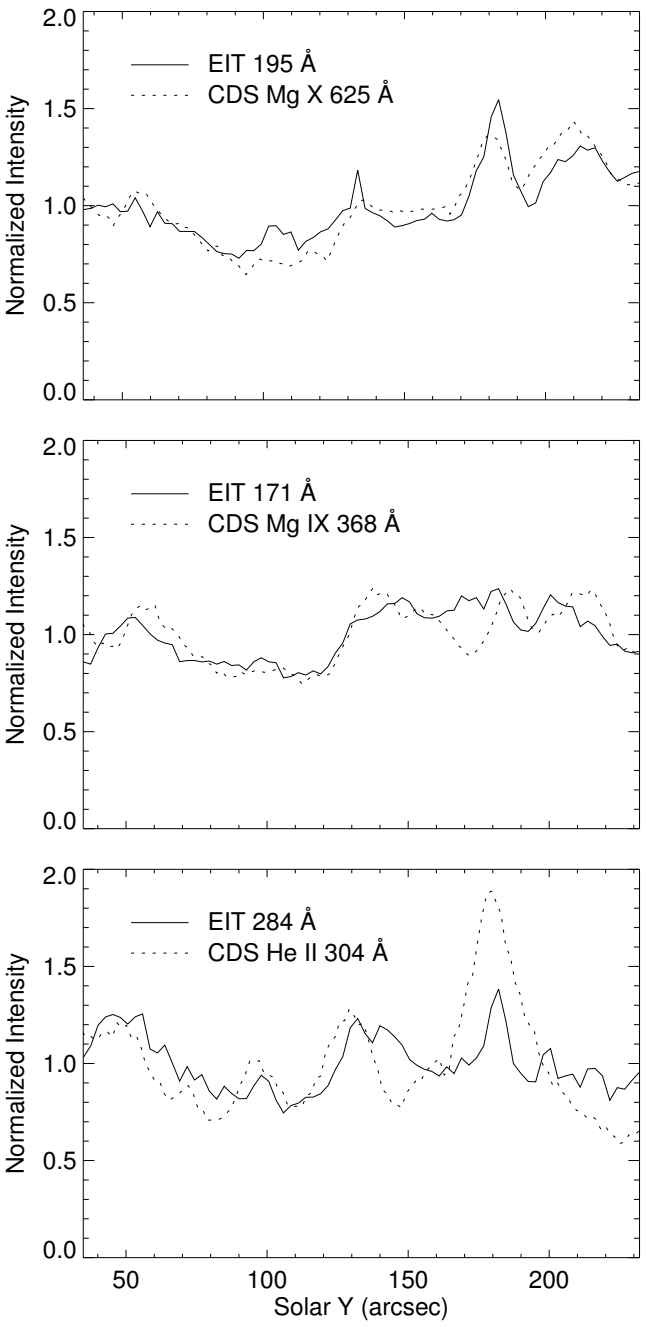

Fig. 3.— Plots of intensity as a function of position along the slit for the CDS field of view. The intensities are determined from averaging across the x direction of the raster. The intensities are normalized by their average values in the field of view.

issues is given in §8.1. We adopted the coronal elemental abundances from the CHIANTI database throughout this work (Feldman et al. 1992).

4. Coronal Diagnostic Spectrometer

4.1. Data Reduction

CDS/NIS data require removal of the CCD bias voltage added to the signal to ensure positivity, cleaning for cosmic ray strikes on the CCD, correction for flat-fielding and non-linearity in detector response, and correction for the effects of the 'burn-in' because of strong lines appearing at the same location on the detector. We also require to convert the photon event count rates to physical units by applying the instrument radiometric calibration. In this work we have used the CDS software routines VDS_DEBIAS, CDS_NEW_SPIKE, and NIS_CALIB to take account of these different effects. Furthermore, we have applied the 2nd order intensity calibration to the appropriate lines around 304 Å. The data were then averaged over the 10 raster positions and along the y-direction of the slit to obtain a composite spectral atlas for analysis.

4.2. Spectral Line Intensities

We used the CDS/NIS spectral atlas of Brooks et al. (1999) and Table 1 of Warren (2005) to identify 54 emission lines in the temperature range $\log T_e = 4.55$ to 6.25. The line profiles were fitted with Gaussians using the ADAS maximum likelihood line fitting procedure ADAS-602. The background was treated either as constant or with a linear slope. The CDS/NIS line widths are dominated by the instrumental widths, so in the wavelength intervals of interest the widths of all the lines were fixed to be the same. However, the precise measurements can show small differences, so we allowed the code to fit the widths rather than impose a single value.

The results are shown in Table 1 which gives the wavelength, formation temperature (from Brooks et al. 1999), and line intensities with uncertainties from the fitting procedure.

4.3. Differential Emission Measure

The intensity of an optically thin emission line corresponding to the transition from level i to level j can be written as

$$I_{i\to j} = A(Z) \int_{T_e} G_{i\to j}(T_e, N_e)\phi(T_e)dT_e \qquad (1)$$

where $A(Z)$ is the elemental abundance, T_e is the electron temperature, and N_e is the electron density. $G(T_e, N_e)$ is the contribution function that contains all of the relevant atomic physics coefficients including any constant factors, and $\phi(T_e)$ is the differential emission measure (DEM) in temperature. In order to define the equation in this form, we assume a constant pressure relationship between density and temperature.

The G function is strongly peaked in temperature but is also sensitive to density through both the population structure of the ion and the ionization balance (Jordan 1969; Summers 1972). A short discussion of this issue is given below (§8.1). Although we have noted this density dependence explicitly, in practise the function is calculated at a single density value derived from e.g. diagnostic line ratios.

4.3.1. Method

Following Warren (2005) we represent the emission measure curve with a series of spline knots which are interactively repositioned to allow more control over the smoothness of the emission measure. The magnitudes of these knots are determined from a χ^2 minimization of the differences between the observed and DEM predicted intensities. This method was found to be useful for obtaining a better representation of the rapid fall off of emission measure at high temperatures, which was difficult to reproduce with other DEM routines. For our initial DEM anal-

ysis, we used $G(T_e, N_e)$ functions calculated from the CHIANTI database.

4.3.2. Coronal Electron Pressure

We assume a uniform electron pressure for the quiet Sun corona in order to calculate the contribution functions necessary for the DEM analysis. The electron pressure estimate is obtained from density sensitive line intensity ratios.

First we examined the ratio of the intensities of the Si IX lines around 350 Å and 345 Å. The numerator is a composite of the transitions $2s^2 2p^2\ ^3P_2 - 2s2p^3\ ^3D_{1,2,3}$ that correspond to emission lines at 349.62 Å, 349.791 Å, and 348.86 Å. The denominator is a composite of the transitions $2s^2 2p^2\ ^3P_1 - 2s2p^3\ ^3D_{1,2}$ that correspond to emission lines at 344.954 Å and 345.120 Å. This ratio is sensitive to electron density in the range of interest for the quiet Sun (Young 2005).

From Table 1 we can see that the observed intensity ratio is 0.84. We used the CHIANTI and ADAS databases to derive the electron density, and obtained values of 2.5×10^8 cm^{-3} and 3.6×10^8 cm^{-3}, respectively. These results translate to electron pressures of $\log P_e = 14.5$ and 14.6, respectively, which are in good agreement with the results of Warren (2005) and Young (2005) who both obtained values of $\log P_e = 14.5$ using the CHIANTI database.

As a further check, we also examined the ratio of intensities of the Si X 356.029 Å and 356.024 Å blended lines, corresponding to the transitions $2s^2 2p\ ^2P_{3/2} - 2s2p^2\ ^2D_{3/2,5/2}$, to the Si X 347.408 Å line corresponding to the $1/2 - 3/2$ transition within the same terms. The observed ratio from Table 1 is 0.59, which translates to an electron density of 3.5×10^8 cm^{-3} and hence an electron pressure of $\log P_e = 14.6$. This is in good agreement with the results obtained for Si IX, and also the result of Warren (2005) who obtained a value of 14.6 for this ratio.

Henceforth, we adopt an electron pressure of $\log P_e = 14.5$ for the DEM analysis. This same value will be used for calculating the updated EIT and TRACE response functions (§5.2 and 6.2), and for calculating the composite radiated power loss curve (see §9.1).

4.3.3. Line selection

We used 38 of the 54 lines listed in Table 1 for the DEM analysis. The excluded lines can be identified from Table 1 because they do not have predicted intensities. They were not used for the following reasons.

1) He I and He II lines. These lines are expected to be affected by opacity, and so the DEM method is not applicable.

2) Si XI 580.920 Å, Mg X 609.786 Å, and Ne V 358.455 Å. From a quick reference check with the CHIANTI database, these lines appear to be strongly affected by blends due to lines from O II, O IV, and Fe X, respectively. The last two blends were also noted by Brooks et al. (1999). A first trial DEM run found that these blends are in fact the main contributors at these wavelengths.

3) Mg VII 365.210 Å, Mg VIII 317.008 Å, Mg VIII 339.000 Å, Fe X 345.735 Å, Fe X 365.565 Å, Fe XII 346.857 Å, and Fe XIII 320.800 Å. In an attempt to standardize our data reduction and analysis procedures we compared line intensities derived from the ADAS-602 fitting procedure with those obtained independently from another line fitting routine (Warren 2005). Before the benchmark comparison, observational data were calibrated and processed independently. We found that the line intensities derived from the two independent methods agreed to within 20% for all the lines used in our study. However, the intensities derived for these 7 lines were different by 22–43%. These differences are because these lines are weak, or blended, or because of ambiguities in background treatment e.g. whether to fit a constant or linear background. The lines can be brought into agreement if we consider the uncertainties in the fitted intensities. However, we excluded them from the analysis since we cannot expect to achieve 20–25% cross-calibration accuracy after including all the atomic data uncertainties etc., if some of the line intensities cannot be measured to this level.

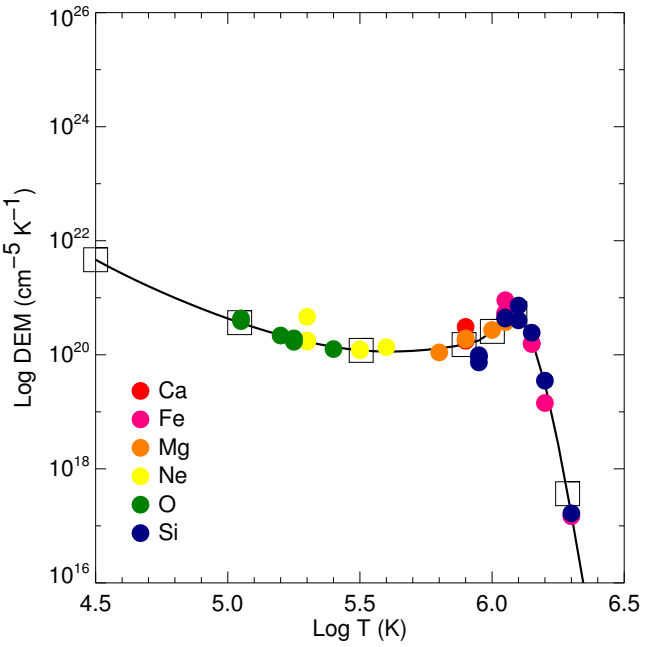

Fig. 4.— The best-fit differential emission measure solution.

4.3.4. Result

Figure 4 shows the computed DEM solution. The boxes show the positions of the 7 spline knots used. As in Warren (2005) we found it necessary to use 4 closely spaced knots between $\log T_e = 5.8$ to 6.3, in order to correctly handle the rapid decrease in emission measure above $\log T_e = 6.0$. The color coded dots show the ratio of the observed to predicted intensities scaled by the emission measure and plotted at the formation temperature of the line.

It can easily be seen that it is difficult to reconcile all of the Fe and Si lines; the Si lines tend to produce higher emission measures above $\log T_e = 6.1$ and lower emission measure below. Furthermore, it is difficult to reconcile these lines with the Mg lines without a fairly sharp peak in the distribution at these temperatures. Warren (2005) addressed this problem by slightly decreasing the elemental abundance for Mg by 10% and increasing the abundance for Si by 30%. We found that this dataset was better fitted by adjusting the Fe and Si abundances upward by 10% and 40%, respectively. Therefore, we used the CHIANTI coronal abundances for all elements except Fe and Si for which we adopted values of 1.38×10^{-4} and 1.78×10^{-4}, respectively.

used were the same as the

Table 1 shows that only 7 of the lines are reproduced to worse

than 50% with the majority reproduced to around 20% or better. At the lower temperatures the distribution is very well constrained, with 14 of the 15 Ne and O lines used in the DEM calculation reproduced to within 20% or better.

4.3.5. Discrepancies between theoretical and observed intensities

From Figure 4 it can easily be seen which lines are not well reproduced by the emission measure curve. Here we discuss those lines reproduced to 50% or worse.

1) The N-like Si VIII lines at 314.345 Å, 316.220 Å, and 319.839 Å are observed to be much weaker than the DEM predicts. Warren (2005) and Landi et al. (2002) have both noted discrepancies for these lines. The latter suggested that this may be because of the neglect of resonances in the collisional excitation rates for transitions within the ground configuration. However, data from Bhatia & Landi (2003) have been included in version 4 of the CHIANTI database, and these data include effective collision strengths from Bell et al. (2001). Bell et al. (2001) state that they have included the effects of resonances in the collisional excitation rates for the ground configuration so this discrepancy remains to be resolved. Interestingly Lanzafame et al. (2005) found no discrepancies for these lines in their analysis of CDS data using ADAS. The different atomic data used in that study may provide an explanation (see §8).

2) The N-like Ne IV 357.889 Å line is a factor of 2.5 more intense than predicted by the DEM. This line is blended with Ne V 357.946 Å according to Brooks et al. (1999) and may be further blended with other lines according to Lanzafame et al. (2005). As with the Si VIII lines there may also be inaccuracies in the collisional excitation rates for this ion.

3) The S-like Fe XI 341.114 Å line is observed to be about 2 times more intense than the DEM predicts. A similar disagreement between theory and observation was noted by Warren (2005) and Landi et al. (2002). However, good agreement for this line was found by Young et al. (1998). Brooks et al. (1999) flagged a possible unknown blend for this line because the position pattern was somewhat different from those of other lines of this ion. Lanzafame et al. (2005) supported this argument with their finding that the Fe XI 341.114/352.661 line ratio was approximately a factor of 2.7 too high. One possible explanation for the discrepancy with the Young et al. (1998) results is that the unknown blend is a lower temperature line that effectively contributes nothing to the hotter active region SERTS spectrum analyzed by those authors.

4) The Si-like Fe XIII 348.182 Å line is overestimated by the DEM by a factor of 2. Discrepancies for this line were also noted by Warren (2005) and Lanzafame et al. (2005). Brooks et al. (1999) suggest that this line may have an unknown blend as well, but it is difficult to confirm this since the DEM predicts a larger intensity than observed. These results are similar to results in Lanzafame et al. (2002) who found a systematic overestimation of the Fe XIII lines used in their DEM study of SERTS observations. They attributed these differences to inaccuracies in the ionization/recombination cross-sections for this ion.

5) The B-like Si X 356.027 Å line is observed to be about 50% more intense than the DEM predicts. A 40% discrepancy was previously noted by Warren (2005) and these results suggest the presence of a blend with this line.

6) The Na-like Ca X 574.007 Å line is observed to be about 2 times more intense than the DEM predicts. Lanzafame et al. (2005) suggest the presence of a weak blend for this line and the CHIANTI database finds an O III line at 574.065 Å which may contribute to this line. This line would have to be a significant contributor to bring the observed and predicted Ca X intensities into agreement. Another possible explanation is that problems with Li-like and Na-like lines have been reported previously by many authors (Dupree 1972; Judge et al. 1995) and it has been suggested that dynamic effects may be responsible because of the long recombination times to the Li-like and Na-like ions. Recently, Doyle et al. (2005) also showed that the contribution functions for several Li-like lines from light elements can be enhanced by significant amounts when a consistent treatment of metastable states and dielectronic recombination is made in the calculations. For example, they found enhancements for the Li-like C IV 1548 Å line of 60% at $\log N_e = 9.0$, rising to a factor of 3 at $\log N_e = 12.0$. A similar examination for the Ca X 574.007 Å line at the appropriate electron density for our observations awaits higher quality atomic data for this element.

5. Transition Region and Coronal Explorer

5.1. Intensities

The TRACE data were reduced using standard analysis procedures in SolarSoft. An area of the images corresponding to the CDS FOV was then extracted and averaged to obtain count rates. Figure 2 shows TRACE 171 Å, 195 Å, and 284 Å images with the extracted CDS area outlined as a box. The average intensity per full resolution pixel is also given.

5.2. Response functions

The TRACE responses as a function of electron temperature can be written as

$$K_{\lambda_0}(T_e) = \int E_{\lambda_0}(\lambda) G(\lambda, T_e) d\lambda \qquad (2)$$

where E_{λ_0} is the response of a particular channel as a function of wavelength and G represents a solar spectrum calculated at a fixed electron density or pressure. We thus assume a relationship between density and temperature.

We calculated new response functions for each channel using the CHIANTI database to compute an isothermal spectrum. These functions are archived within the standard SolarSoft library for different combinations of elemental abundances (Anders & Grevesse 1989; Feldman et al. 1992) using the ionization fractions of Mazzotta et al. (1998). They were computed for electron densities of 10^8 cm^{-3} and 10^9 cm^{-3}, and electron pressures of 10^{15} cm^{-3} K and 10^{16} cm^{-3} K.

Adopting the line ratio results of §4.3.2, we also computed the response functions for an electron pressure of $10^{14.5}$ cm^{-3} K for use in this work. These curves are to be used together with the DEM analysis results to predict the TRACE count rates. Therefore, to maintain consistency in the atomic data used for these computations, we modified the elemental abundances used in the response calculations in the same way that they were modified for obtaining the best fit DEM (see §4.3.4).

Figures 5–7 contrast these new response functions with the previous functions archived in the SolarSoft library for a pressure of 10^{15} cm^{-3} K. The lower panels in each figure show the percentage differences between the old and new curves against temperature.

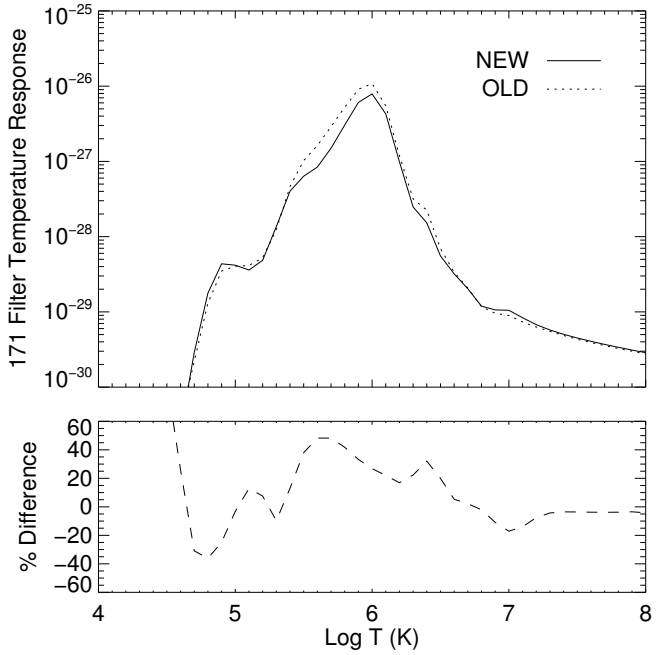

Fig. 5.— Upper panel: Temperature response of the 171 Å channel compared to the previous file in the TRACE archive. Solid line - new calculation for an electron pressure of $\log P_e = 14.5$. Dashed line - old calculation for an electron pressure of $\log P_e = 15.0$. Lower panel: Percentage differences against temperature.

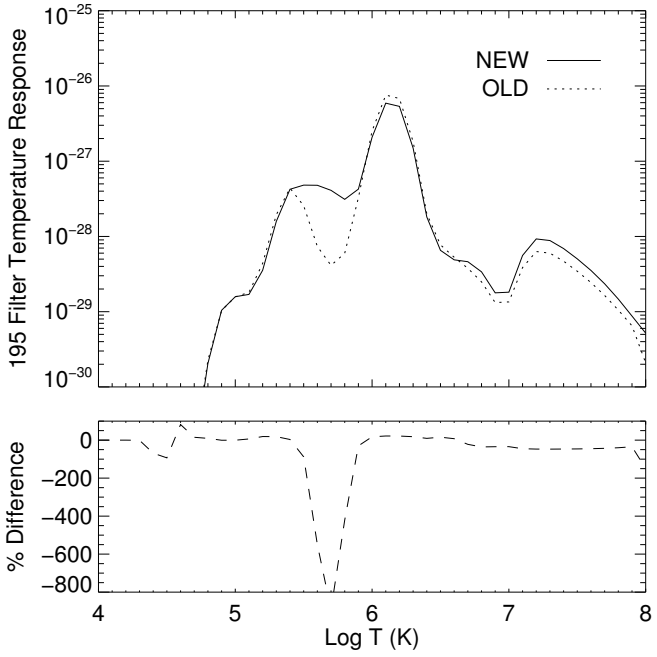

Fig. 6.— Upper panel: Temperature response of the 195 Å channel compared to the previous file in the TRACE archive. Solid line - new calculation for an electron pressure of $\log P_e = 14.5$. Dashed line - old calculation for an electron pressure of $\log P_e = 15.0$. electron pressure of $\log P_e = 14.5$. Lower panel: Percentage differences against temperature.

For the 171 Å channel the peak decreases by 27% at $\log T_e$=6.0, and there are differences of $\sim$ 35–50% above $\log T_e$=4.6. Below this temperature the differences increase as the curves fall rapidly at low temperature.

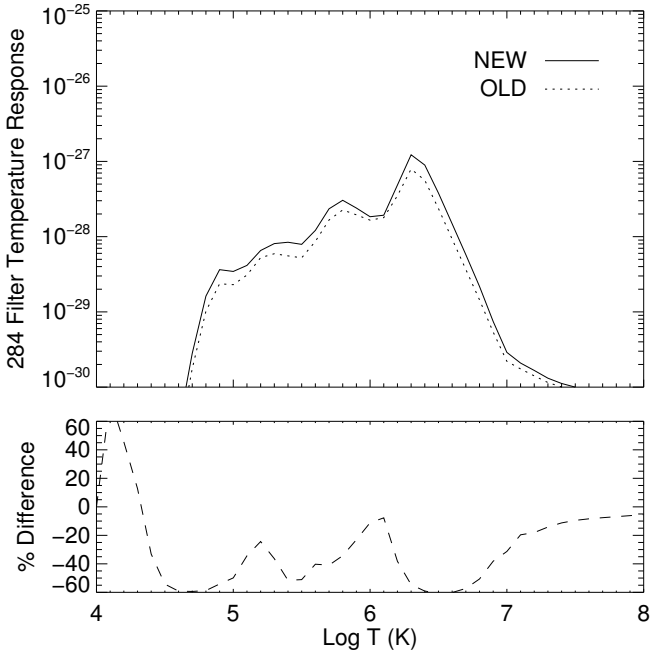

Fig. 7.— Upper panel: Temperature response of the 284 Å channel compared to the previous file in the TRACE archive. Solid line - new calculation for an electron pressure of $\log P_e = 14.5$. Dashed line - old calculation for an electron pressure of $\log P_e = 15.0$. electron pressure of $\log P_e = 14.5$. Lower panel: Percentage differences against temperature.

For the 195 Å channel the peak decreases by 22% at $\log T_e$=6.1, and there is a substantial difference of a factor 10 at $\log T_e$= 5.7. As pointed out by Del Zanna & Mason (2003), this is due to an increased contribution from Fe VIII 185.213 Å close to this temperature in the latest version of the CHIANTI database. For the 284 Å channel the peak increases by 55% at $\log T_e$= 6.3, and there are differences of 5–60% above $\log T_e$= 4.5. The differences increase also in this case at lower temperatures.

6. Extreme ultraviolet Imaging Telescope

6.1. Intensities

The EIT data were reduced using standard analysis procedures in SolarSoft. An area of the images corresponding to the CDS FOV was then extracted and averaged to obtain count rates. Figure 2 shows EIT 171 Å 195 Å and 284 Å images with the extracted CDS area outlined as a box. The average intensity per full resolution pixel is also given.

6.2. Response functions

The EIT response functions can be expressed as in equation (2). We used the isothermal spectra computed for TRACE using the CHIANTI database to calculate the EIT responses for each wavelength channel as a function of temperature. Figures 8–11 show these new response functions for a pressure of $10^{14.5}$ cm^{-3} K. As with TRACE, we maintained consistency between the atomic data used by adjusting the elemental abundances in the same way they were adjusted to obtain the best DEM solution (§4.3.4). The equivalent TRACE response functions have been scaled approximately by the ratio of the peaks and overlaid for comparison.

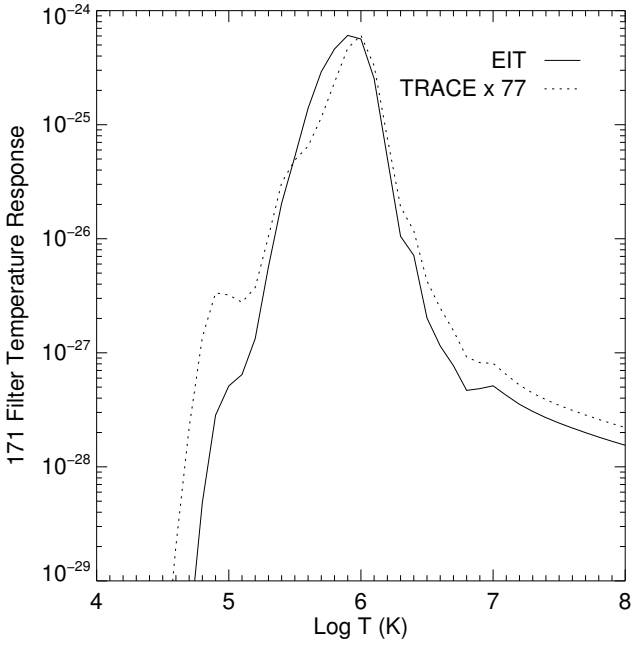

Fig. 8.— Temperature response of the EIT 171 Å channel (solid line). The scaled equivalent TRACE response is overlaid as a dotted line.

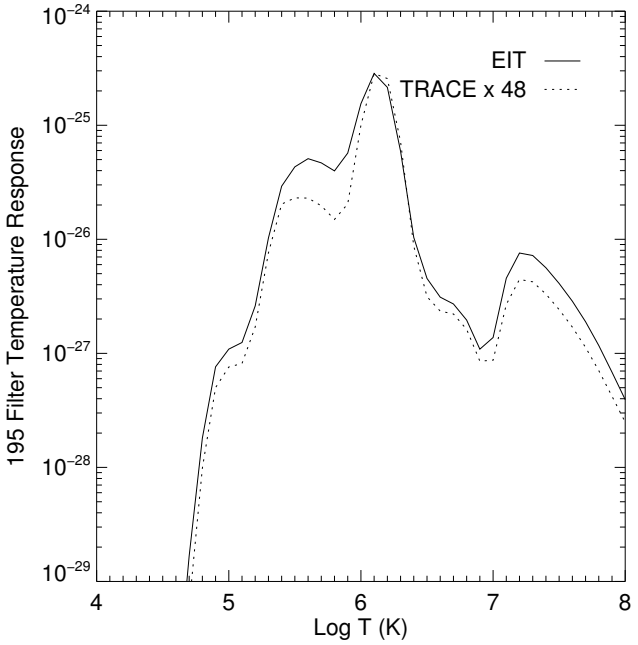

Fig. 9.— Temperature response of the EIT 195 Å channel (solid line). The scaled equivalent TRACE response is overlaid as a dotted line.

Comparing with the response curves presented in Figure 12 of Dere et al. (2000), our responses for the 171 Å, 195 Å, and 284 Å channels appear to have increased significantly. If we take ratios of the maximum responses of our new calculations with the maximum values given in Tables x–xii of Dere et al. (2000), we find values of 3.50, 3.11, and 3.18 for the 171 Å, 195 Å, and 284 Å channels, respectively. Dere et al. (2000) used the elemental abundances of Meyer (1985) in their study, who gives a value of 3.89×10^{-5} for Fe which is the main contributor in each of the channels. Zhang et al. (2001) — including K. Dere as co-author

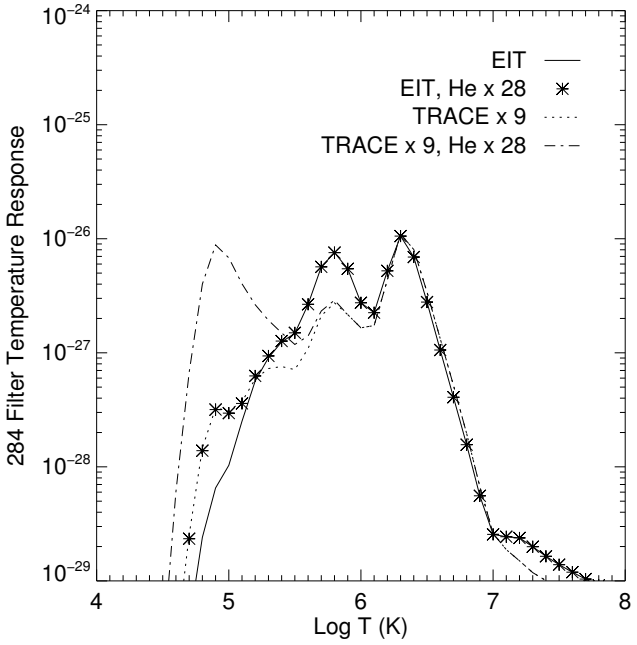

Fig. 10.— Temperature response of the EIT 284 Å channel (solid line). The scaled equivalent TRACE response is overlaid as a dotted line. Also overlaid are the two curves after approximate correction for the contribution of the optically thick He II 304 Å line (see §7).

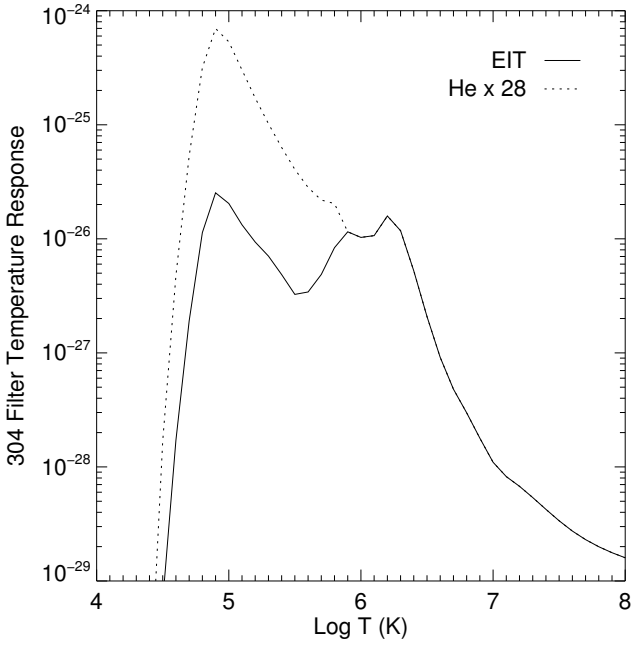

Fig. 11.— Temperature response of the EIT 304 Å channel (solid line). The overlaid dotted line is the response with an approximate correction for the contribution of the optically thick He II 304 Å line (see §7).

— later argue that this value is about a factor of 2 too small, and revise the Fe abundance upwards to 6.31×10^{-5}. In the present work, we have used the CHIANTI data including the results of Feldman et al. (1992) adjusted upwards by 10% (see §4.3.4). That is, we have used a value for Fe of 1.38×10^{-4}. This is a factor of 3.55 larger than the value given by Meyer (1985), which is sufficient to explain the increases found in Figures 8–10.

For the 304 Å channel the difference is much smaller. In comparison with the results of Table XIII of Dere et al. (2000) our response function has decreased by about 33%. Approximately 20% of this difference can be accounted for by the different values adopted for the He abundance; Meyer (1985) gives an abundance value of 0.098 whereas CHIANTI gives a value of 0.079.

Note also the lack of a dip around $\log T_e = 5.7$ in the 195 Å response function plot when compared to the Dere et al. (2000) figures. This is again due to the improved treatment of Fe VIII in the latest version of the CHIANTI database.

7. Comparison of EIT and TRACE intensities with those predicted by the CDS DEM

To obtain the actual TRACE and EIT count rates, we convolve the new response functions calculated in §5.2 with the DEM distribution obtained in §4.3.4 from the simultaneous CDS/NIS observations thus

$$I_{\lambda_0} = \int K_{\lambda_0}(T_e)\phi(T_e)T_e dlnT_e \quad (3)$$

where $\phi(T_e)$ is the DEM. The results are shown in Table 2. Note again that the response functions were modified to account for the Fe and Si abundance adjustments in §4.3.4.

For the TRACE 171 Å channel the method predicts the count rates to within $\sim$ 2%. For the 195 Å channel the prediction is within $\sim$ 40%. This latter prediction comes within 26% if the extra adjustment to the abundances is not made in the response functions. These results suggest that the TRACE calibration is good for these filters. For the EIT 171 Å channel the method predicts the count rates to within $\sim$ 26%. For the 195 Å channel the prediction is better and within $\sim$ 5%. So the TRACE result is better for the 171 Å filter, and the EIT result is better for the 195 Å filter.

The TRACE 284 Å filter predicted count rate is, however, only about 1/5th of that observed. For EIT the predicted count rate is about 2/5th of that observed. These results are worse than for the 171 Å and 195 Å filters partly because the He II lines at $\sim$ 304 Å contribute significantly in these pass-bands, and their emission is not adequately approximated by the optically thin model. These lines are enhanced by several factors in the quiet solar atmosphere (Jordan 1975). In fact the prediction for the 304 Å EIT channel is the worst of all the channels.

To try to account for the He contribution we included the 304 Å line in our DEM analysis and used the solution from §4.3.4 to predict its intensity. We found that the DEM predicted intensity was a factor of 28.3 lower than that observed! Therefore, we scaled the He II 304 Å $G(T_e, N_e)$ function by this factor and used it in our calculation of the synthetic spectrum. We then convolved this new spectrum with the EIT and TRACE response curves and used the CDS DEM to estimate the new count rates in the EIT and TRACE channels. The results are also shown in Table 2. The 171 Å and 195 Å channels are not significantly affected by the change for EIT or TRACE. However, although the adjustment increases the count rate for the 304 Å channel by a factor of $\sim$ 7, it does not affect the EIT 284 Å count rate prediction and only increases the prediction for the TRACE 284 Å channel from 0.06 to 0.10 DN s^{-1} pix^{-1}. Interestingly, this brings the TRACE discrepancy into close agreement with the EIT discrepancy. However, the prediction for the 304 Å channel is still less than half of that observed.

Finally, as a test, we scaled the He II 304 Å $G(T_e, N_e)$ function by the factor required to bring the EIT 304 Å channel count rate prediction into agreement with the observations. Even in this scenario the EIT 284 Å predicted count rate was not significantly affected, and the TRACE 284 Å predicted count rate did not increase sufficiently to remove the discrepancy. These results indicate not only that the He II 304 Å line formation is not well understood, but that there are significant problems in understanding and interpreting the emission in the EIT and TRACE 284 Å channels. This could be because of calibration problems, or the absence of important lines in this wavelength range in the CHIANTI database, or scattered light issues, or a combination of all of these.

8. Discussion of atomic physics issues

8.1. Atomic modeling of finite density plasmas

As mentioned in §4.3, the $G(T_e, N_e)$ functions used in the DEM analysis are strongly dependent on temperature but are also sensitive to electron density. This is because of the competition of collisional and radiative processes establishing the ionization state of the element and population density of the level emitting the line. Usually in the astrophysical literature the competition between the various processes is only partially included in the atomic models. For example, in most atomic databases the density sensitivity of the ionization balance is ignored. This results in an inconsistency in the atomic modeling where a collisional-radiative approximation is used for the level population calculations, but a coronal (zero density) approximation is used for the ionization fractions. However, dielectronic recombination, which is the dominant electron-ion recombination mechanism in the low density corona (Burgess 1964), can be collisionally disrupted before stabilization has taken place at only moderate densities. This results in a suppression of the effective dielectronic recombination rate coefficient that in turn makes ionization fractions sensitive to electron density (Burgess & Summers 1969). Furthermore, dielectronic recombination into highly excited states affects the level population calculations (Badnell et al. 2003).

A further complication results from the role of metastable states. As the electron density increases, collisional deexcitation eventually overcomes spontaneous radiative decay as the principal deexcitation mechanism. For metastables, whose transition probabilities are much lower than for ordinary excited levels, this can take place at quite low densities. They can therefore attain substantial populations. For example, for O III, lines of which are found in the spectrum analyzed in this paper, about 25% of the total ionization stage population is found in the $2s^2 2p^{2\,1}D$ metastable term at $\log N_e = 9.5$ cm^{-3}. It thus becomes a source term for dielectronic recombination and ionization at densities comparable to the ones found in this paper, assuming the coronal electron pressure derived in §4.3.2 is representative of the pressure at the formation temperature of O III. With more elaborate GCR (Generalized Collisional-Radiative, Summers et al. 2005) models these effects can be examined in detail, and the highest quality state selective dielectronic recombination data can be included (Badnell et al. 2003).

It turns out that even approximate scaling of the density dependence of the ionization fractions when combined with density dependent excited population calculations can reveal interesting consequences under certain conditions. For example, Lanzafame et al. (2002) showed that spurious multiple peaks would appear

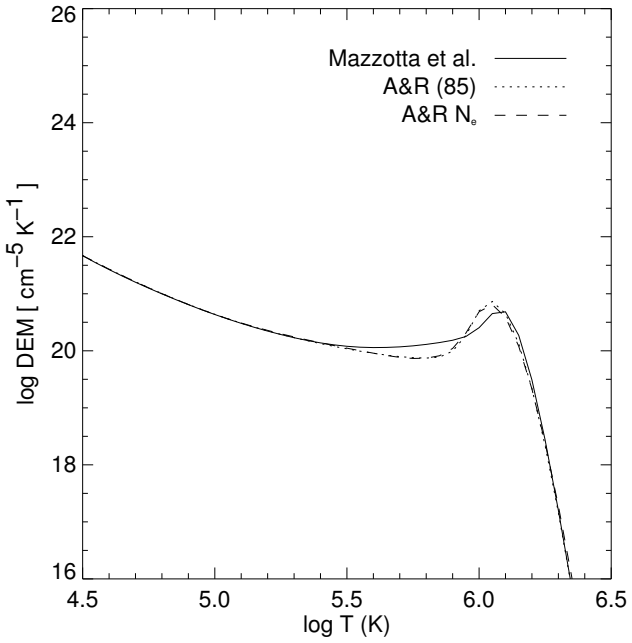

Fig. 12.— Comparison of DEM solutions for three sets of ion fractions. Solid line - Mazzotta et al. (1998). Dotted line - Arnaud & Rothenflug (1985). Dashed line - Arnaud & Rothenflug (1985) at $logP_e = 14.5$ cm^{-3} K.

in their active region coronal DEM distribution, derived from SERTS data, if they mimicked the effect of using low density contribution functions in their computations.

The data analyzed in the present work are consistent with a quiet Sun region with a low electron pressure of $10^{14.5}$ cm^{-3} K (a factor $\sim$ 10–20 lower than in Lanzafame et al. 2002). Therefore, such effects are expected to be less significant here. However, in order to explore some of the differences, we have considered the consequences of using approximately scaled density dependent ionization fractions in our DEM analysis. We have not considered the influence of metastables.

8.2. Implications for the DEM distribution

We computed the DEM curve at the constant electron pressure derived from the diagnostic line ratios, i.e. $10^{14.5}$ cm^{-3} K, using the Arnaud & Rothenflug (1985) data scaled for electron density as in Summers (1974). We used density scaled Arnaud & Raymond (1992) data for Fe. We adopted the solution from §4.3.4 as a starting guess, and modified the spline to best fit the new data. Since the ionization fractions are different for the two DEMs we computed a third DEM using the Arnaud & Rothenflug (1985) data computed at an electron density of 10^4 cm^{-3}. This curve represents the low density limit and allows us to distinguish between differences due to the different ion fractions or the density effects. Henceforth we refer to the solution from §4.3.4 as DEM1, the new low density case using the Arnaud & Rothenflug (1985) data as AR1, and the solution at $10^{14.5}$ cm^{-3} K as AR2.

Figure 12 contrasts the two best-fit DEM solutions AR1 & AR2 with DEM1. The results are qualitatively similar, but it is noticeable that a sharper peak around $\log T_e = 6.05$ is needed in the two new cases to reproduce the Mg lines and reconcile them with the Fe and Si lines.

There is less scatter in the AR2 results for lines of these elements compared to DEM1 (excluding Mg X), and the Fe and Si lines are in better agreement. So we saw no justification for adjusting their abundances in this case. There is considerably more scatter in the results for the lines of O and Ne, and the Ca lines are not reproduced well. However, the majority of the lines are reproduced to better than 20% with only 8 reproduced to worse than 50%. This is comparable to the results for DEM1 especially when you consider that the abundances have not been adjusted in this case.

The AR2 solution appears slightly better at reproducing the line intensities more often than AR1 (55% of the time), and the scatter in the results for the Fe, Mg, Ne, and Ca lines is also worse in the low density case. This means that additional Fe and Mg lines are reproduced better with the DEM1 case when compared to AR1, than when compared to AR2. Otherwise, there does not appear to be a significant difference between the AR1 & AR2 results. This suggests that the major difference in the DEM distributions is mainly caused by the ion fraction datasets, and that the density dependence is mainly important when considering the fine details of individual line discrepancies, at least in the case of this quiet coronal low pressure region.

8.3. Implications for discrepant lines

We revisit some of the discrepant lines from §4.3.5 with the new results. The results do not provide any additional information for the Fe XI 341.114 Å, Fe XIII 348.182 Å, and Ne IV 357.889 Å lines so these are not discussed further.

The N-like Si VIII lines at 314.345 Å, 316.220 Å, and 319.839 Å were observed to be much weaker than predicted by DEM1. However, this discrepancy was not seen by Lanzafame et al. (2005) in their analysis of CDS data. In case AR2, these lines are reproduced to within 10%, 17%, and 46%, consistent with the Lanzafame et al. (2005) results who also used Arnaud & Rothenflug (1985) and Arnaud & Raymond (1992) density scaled data in their analysis. In case AR1 they are reproduced to within 14–53% suggesting that the cause of the discrepancy found by Warren (2005) and Landi et al. (2002) is the Mazzotta et al. (1998) data for the Si VIII ion fractions.

In fact, the agreement for the B-like Si X 356.027 Å line improves slightly as well. The observed intensity was about 50% greater than predicted by DEM1 where the Si abundance was adjusted, and is 49% greater in this case without changing the abundances.

The Na-like Ca X 574.007 Å line was observed to be about 2 times more intense than predicted by DEM1. In case AR2 the situation is worse: the observed intensity is 5 times greater than the predicted one, and the Ca X 557.759 Å line is also now 3 times weaker than observed. These large discrepancies are most likely because of the difference in ionization fractions used.

Three additional lines are reproduced to worse than 50% in case AR2: Mg X 624.95 Å, Ne VI 558.591 Å, and Si XI 303.326 Å. Each of these lines is the only one observed from that ion, and since they were reproduced well by DEM1 it suggests that the ion fractions are the sources of the discrepancies in these cases also.

8.4. Implications for the EIT and TRACE count rate predictions

Using the two new DEM solutions we recomputed the EIT and TRACE count rates for each channel including the adjustment

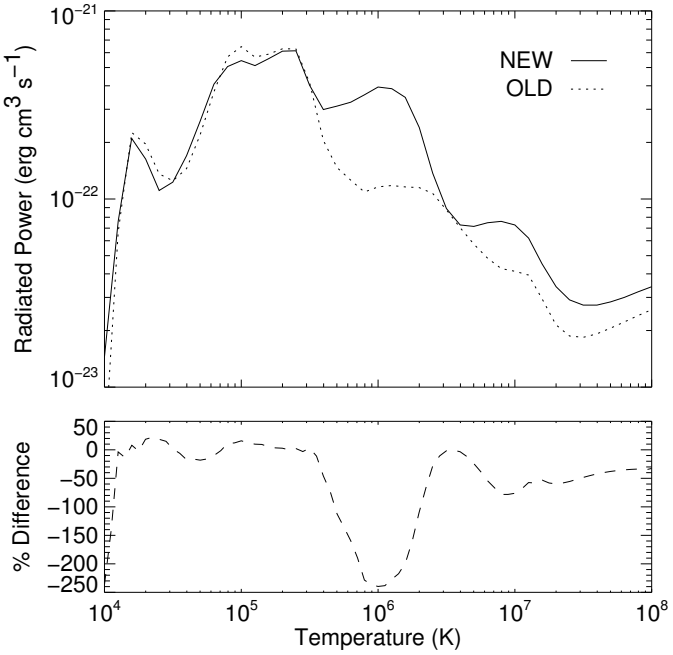

Fig. 13.— Upper panel: Composite radiated power loss function calculated for an electron pressure of $\log P_e = 14.5$ (solid line) compared to the previous function used in our hydrodynamic simulations. Lower panel: The percentage differences between the two curves against temperature.

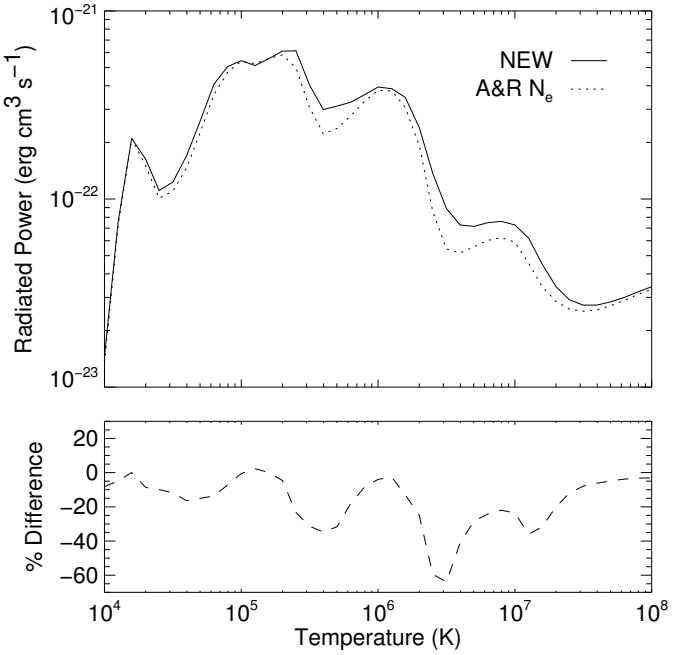

Fig. 14.— Comparison of composite radiated power loss function and the result using the Arnaud & Rothenflug (1985) and Arnaud & Raymond (1992) data scaled to the appropriate electron density.

for the He II 304 Å lines discussed in §7. The results are also shown in Table 2.

For TRACE, the new solutions produce worse agreement for the 171 Å and 284 Å channels but better agreement for the 195 Å channel. In the latter case the low density solution is within 4%. The improvement for the 195 Å channel and worsened disagreement for the 171 Å channel may reflect the fact that the DEM solution is better constrained at temperatures above $\log T_e = 6.0$ in the density dependent cases. The main contributor in the 171 Å pass band (Fe IX) is formed below this temperature ($\log T_e = 5.8$), whereas the main contributor in the 195 Å pass band (Fe XII) is formed above this temperature ($\log T_e = 6.15$).

For EIT, the agreement is better for the 284 Å filter using DEM1 and the results are comparable between the different solutions for the 304 Å channel. However, AR1 produces the best agreement for the 171 Å channel (within 19%) and AR2 produces the best agreement for the 195 Å channel (within 4%).

It is interesting to note that including the density scaling in the ion fractions increases the 195 Å channel predicted count rate for EIT and TRACE by ∼20–40%, and reduces the 171 Å channel predicted count rate for both instruments by ∼ 8%. Similar increases and decreases might be expected in the DEM1 predictions using the Mazzotta et al. (1998) data if a similar density scaling were applied. In such a case, the predicted count rates using the Mazzotta et al. (1998) data would give worse disagreement than AR1 & AR2 except for the TRACE 171 Å pass band.

9. Application of the results to hydrodynamic modeling

9.1. Radiated Power Loss

One of the goals of the present work was to attain consistency between all the atomic data going into the complete cycle of analysis. That is, from DEM, synthetic spectra, TRACE and EIT response functions, to the radiative loss curves which are input into our hydrodynamic simulations. Therefore, for comparison with previous hydrodynamic work (e.g., Warren et al. 2003), we computed a new composite radiated power loss function, $\Lambda(T_e, n_e)$, for the quiet Sun atmosphere at an electron pressure of $\log P_e = 14.5$, using the latest CHIANTI data and adjusted abundances of §4.3.4. This function can be combined with the emission measure distribution and Hydrogen ionization balance and then integrated in temperature to obtain the total radiated power from the coronal plasma.

Our updated curve $\Lambda(T_e, n_e)$ is shown in Figure 13 as the solid line and the values are listed in Table 3. The previous curve used in our hydrodynamic simulations is shown as the dotted curve and is from Rosner et al. (1978). This curve uses photospheric rather than coronal abundances and this is expected to make a significant difference (Cook et al. 1989). The lower panel in the figure shows the percentage differences between the two curves against temperature. The differences are large below $\log T_e = 4.1$ because of the rapid fall off of the curves below this temperature and the differences in spline treatment. However, the curve is not realistically determined anyway in this temperature range since the effects of opacity are not included. The differences are then up to ∼ 20% below $\log T_e = 5.6$ increasing to about a factor 3.4 at $\log T_e = 6.0$. Above this temperature the differences reduce, but are still up to 80%. Fe is the main contributor to the curve at $\log T_e = 6.0$ and so the large difference here is likely to be because of the adoption of coronal elemental abundances in the new calculations. Low First Ionization Potential (FIP) elements are enriched by several factors in the Feldman et al. (1992) abundances.

As pointed out by Landi & Landini (1999) the details of the radiated power loss function can be affected by the approximations used in the level population calculations, or by different

ionization fraction datasets. Therefore, we also computed the curve including the density dependence of the ionization fractions as discussed in previous sections. The results are shown in Figure 14 and compared to the 'NEW' curve of Figure 13. It can be seen that the differences reach 65% around T_e = 2–3 × 10^6 K. By comparison with the low density case using the Arnaud & Rothenflug (1985) data, we estimate that this difference is about 25% smaller as a result of including the density dependence than it would be without. The larger remaining discrepancy is because of the difference in ion fractions used.

These results suggest that the density dependence of the ionization fractions will have some effect. Although we briefly discussed the influence of the highest quality metastable resolved data in §8.1 we did not investigate this issue in detail in the present work. However, Doyle et al. (2005) have recently shown that the effects of including metastable states can *increase* the total radiated power function by 10–20% in the transition region, and *decrease* the function by about 30% above $\log T_e = 6.0$. The largest single uncertainty in the radiated power loss function calculations are the values adopted for the elemental abundances (Summers & McWhirter 1979; Landi & Landini 1999).

10. Conclusions and Discussion

We have analyzed CDS, EIT, and TRACE observations of a quiet coronal region in order to assess the accuracy of the instrument intercalibrations. In doing so we assessed different data reduction procedures, analysis methods, and atomic data. Our objective was to define a standard consistent pathway for analyzing observations from future instruments such as Solar-B/EIS (Extreme ultraviolet Imaging Spectrometer).

We find that the EIT and TRACE 171 Å and 195 Å channel calibrations are generally well understood. Using DEMs derived from coordinated CDS observations we can predict the EIT and TRACE count rates to within 25%. However, the accuracy of the predictions is somewhat dependent on the details of the ionization fractions and elemental abundances used in the DEM analysis. For example, for the TRACE 195 Å channel, using the Mazzotta et al. (1998) ionization fractions and Feldman et al. (1992) elemental abundances adjusted to best-fit the DEM, results in a prediction which is about 39% out. This value can be reduced to about 5% if the Arnaud & Rothenflug (1985) ionization fractions are used.

In general, the different DEM solutions using different ion fractions and abundances produced fairly similar results. The majority of the CDS line intensities were reproduced to within 20% in each case, with only around one fifth of the lines reproduced to worse than 50%. The DEMs derived using Arnaud & Rothenflug (1985) and Arnaud & Raymond (1992) data were more narrowly peaked and showed greater scatter when compared to the DEM derived using the Mazzotta et al. (1998) data (especially in the Ca, Ne, and O lines). On the other hand, they were able to reproduce the Fe, Si, and Mg lines better (except Mg X) without resorting to abundance adjustments.

We examined the reasons for some of the worst discrepancies in §4.3.5, and the analysis pointed out the additional clues and advances made possible by examining different ion fraction datasets. For example, we found evidence that the Arnaud & Rothenflug (1985) data can remove the discrepancies found by previous authors for the Si VIII lines using the data of Mazzotta et al. (1998). Recently, Andretta et al. (2003) also pointed out that the Arnaud & Rothenflug (1985) data produced greater agreement between theory and observations in their analysis of CDS data.

Although the major differences found in our study seem to originate in the choice of ion fraction dataset, the inclusion of the density dependence seems to improve the agreement between theory and observations when compared to the zero density case. The predicted EIT and TRACE count rates for the 171 Å and 195 Å channels are also altered by ± 10–40% when the density dependence is included. If similar alterations were applied to the Mazzotta et al. (1998) DEM predictions, that solution would give the worst agreement for all but the TRACE 171 Å channel.

The TRACE 284 Å and EIT 284 Å and 304 Å filter predictions do not agree at all well with the observations. This is partly because the He II 304 Å lines that contribute to these pass-bands are not adequately approximated by the atomic models used. Adjusting the He II 304 Å $G(T_e, N_e)$ function by a factor sufficient to bring the observed and DEM predicted intensities into agreement results in a prediction for the EIT 304 Å channel count rate which is a factor ∼ 2.4 less than observed. A similar adjustment for the 284 Å channels leaves the TRACE and EIT predictions factors of ∼ 2.8 and 2.6 lower than observed. These discrepancies may be indicative of scattered light issues, calibration uncertainties, or a lack of spectral lines in the atomic database for this region.

A product of our study is a set of new TRACE response functions and synthetic spectra that we have placed in SolarSoft for general use. The spectra and functions are calculated for photospheric and coronal abundances at electron densities of 10^8 and 10^9 cm^{-3} and electron pressures of 10^{15} and 10^{16} cm^{-3} K. In the present work, we studied a coronal region with an electron pressure of $10^{14.5}$ cm^{-3} K. In order to facilitate the calculation of spectra and response functions at this, or any other, electron pressure, we have also placed the IDL routines we used for computing them in SolarSoft.

Another potentially useful application of the DEM method to physical models is the determination of elemental abundances, which give rise to major uncertainties in the radiated power loss calculations. These power loss calculations are important for determining the energy balance in the solar atmosphere through hydrodynamic simulations. We have calculated a new radiated power loss function for use in hydrodynamic simulations, and found that the choice of Mazzotta et al. (1998) or Arnaud & Rothenflug (1985) ion fractions and elemental abundances that best fit the CDS DEM can result in differences of up to ∼ 90% at T_e = 2–3 × 10^6 K. This difference is reduced to about 65% if the density dependence is included in the Arnaud & Rothenflug (1985) data. In general the inclusion of the density dependence appears to improve the agreement between the results of Arnaud & Rothenflug (1985) and Mazzotta et al. (1998).

Finally, note again that we have studied a quiet corona region with a pressure of $10^{14.5}$ cm^{-3} K and thus a low density of ∼ 3 × 10^8 cm^{-3} at coronal temperatures. Density effects will play an increasingly important role as we move to higher densities, and active regions, in the chromosphere and transition region. However, these results highlight the need for accurate equilibrium ionization balance calculations even at low density.

We thank John Mariska for useful suggestions for the manuscript. CDS was built and is operated by a consortium led by the Rutherford Appleton Laboratory and including the Mullard

Space Science Laboratory, the NASA Goddard Space Flight Center, Oslo University and the Max Planck Institute for Extraterrestrial Physics, Garching. The EIT images are courtesy of the SOHO/EIT Consortium. SOHO is a mission of international cooperation between ESA and NASA. The TRACE images are courtesy of the TRACE Consortium. CHIANTI is a collaborative project involving the NRL (USA), RAL (UK), and the Universities of Florence (Italy) and Cambridge (UK). This work was done in the context of the ADAS project.

REFERENCES

Anders, E., & Grevesse, N. 1989, Geochim. Cosmochim. Acta, 53, 197
Andretta, V., Del Zanna, G., & Jordan, S. D. 2003, A&A, 400, 737
Arnaud, M., & Raymond, J. 1992, ApJ, 398, 394
Arnaud, M., & Rothenflug, R. 1985, A&AS, 60, 425
Badnell, N. R., et al. 2003, A&A, 406, 1151
Bell, K. L., Matthews, A., & Ramsbottom, C. A. 2001, MNRAS, 322, 779
Bhatia, A. K., & Landi, E. 2003, At. Data & Nucl. Data Tables, 85, 317
Brooks, D. H., et al. 1999, A&A, 347, 277
Burgess, A. 1964, ApJ, 139, 776
Burgess, A., & Summers, H. P. 1969, ApJ, 157, 1007
Cook, J. W., Cheng, C.-C., Jacobs, V. L., & Antiochos, S. K. 1989, ApJ, 338, 1176
Del Zanna, G., & Mason, H. E. 2003, A&A, 406, 1089
Delaboudiniere, J.-P., et al. 1995, Sol. Phys., 162, 291
Dere, K. P., Landi, E., Mason, H. E., Monsignori Fossi, B. C., & Young, P. R. 1997, A&AS, 125, 149
Dere, K. P., et al. 2000, Sol. Phys., 195, 13
Domingo, V., Fleck, B., & Poland, A. I. 1995, Sol. Phys., 162, 1
Doyle, J. G., Summers, H. P., & Bryans, P. 2005, A&A, 430, L29
Dupree, A. K. 1972, ApJ, 178, 527
Feldman, U., Mandelbaum, P., Seely, J. F., Doschek, G. A., & Gursky, H. 1992, ApJS, 81, 387
Handy, B. N., et al. 1999, Sol. Phys., 187, 229
Harrison, R. A., et al. 1995, Sol. Phys., 162, 233
Harrison, R. A., & Thompson, A. M. 1991, Intensity Integral Inversion Techniques: a Study in Preparation for the SOHO Mission RAL Technical Report, RAL91-092
Jordan, C. 1969, MNRAS, 142, 501
Jordan, C. 1975, MNRAS, 170, 429
Judge, P. G., Woods, T. N., Brekke, P., & Rottman, G. J. 1995, ApJ, 455, L85
Landi, E., Feldman, U., & Dere, K. P. 2002, ApJ, 574, 495
Landi, E., & Landini, M. 1999, A&A, 347, 401
Lang, J. 1994, Atomic Data and Nuclear Data Tables, 57, 1
Lanzafame, A. C., Brooks, D. H., & Lang, J. 2005, A&A, 432, 1063
Lanzafame, A. C., Brooks, D. H., Lang, J., Summers, H. P., Thomas, R. J., & Thompson, A. M. 2002, A&A, 384, 242
Mazzotta, P., Mazzitelli, G., Colafrancesco, S., & Vittorio, N. 1998, A&AS, 133, 403
Meyer, J.-P. 1985, ApJS, 57, 173
Rosner, R., Tucker, W. H., & Vaiana, G. S. 1978, ApJ, 220, 643
Summers, H. P. 1972, MNRAS, 158, 255
Summers, H. P. 1974, Internal Memo, Astrophys. Res. Div. (Appleton Lab., Abingdon, Oxon.), 367
Summers, H. P. 2001, The ADAS manual, version 2-9, http://adas.phys.strath.ac.uk
Summers, H. P., et al. 2005, Plasma Physics and Controlled Fusion, submitted
Summers, H. P., & McWhirter, R. W. P. 1979, Journal of Physics B Atomic Molecular Physics, 12, 2387
Warren, H. P. 2005, ApJS, 157, 147
Warren, H. P., Winebarger, A. R., & Mariska, J. T. 2003, ApJ, 593, 1174
Young, P. R. 2005, A&A, in press
Young, P. R., Del Zanna, G., Landi, E., Dere, K. P., Mason, H. E., & Landini, M. 2003, ApJS, 144, 135
Young, P. R., Landi, E., & Thomas, R. J. 1998, A&A, 329, 291
Zhang, J., Kundu, M. R., White, S. M., Dere, K. P., & Newmark, J. S. 2001, ApJ, 561, 396

TABLE 1
QUIET SUN INTENSITIES FROM THE CDS NORMAL INCIDENCE SPECTROMETER.

Ion	λ_{obs} (Å)	$\log T_{max}$ (K)	I^a_{obs}	I^a_{dem}	Ratio
He I	515.617	4.55	10.62±0.28		
He I	522.213	4.55	18.68±0.34		
He I	537.030	4.55	55.25±1.29		
He I	584.334	4.55	642.45±8.67		
He II	303.780	4.65	3428.00±65.82		
O III	525.797	5.10	17.56±0.38	14.52	0.83
O III	599.598	5.10	35.47±0.70	32.77	0.92
Ne IV	357.889	5.15	5.49±0.42	2.02	0.37
Ne IV	541.126	5.15	2.43±0.12	2.35	0.97
Ne IV	542.070	5.15	4.72±0.13	4.70	1.00
Ne IV	543.886	5.15	7.35±0.17	7.02	0.96
O IV	553.329	5.25	21.43±0.63	21.75	1.01
O IV	554.076	5.25	37.32±2.03	42.50	1.14
O IV	554.513	5.25	103.20±2.17	109.06	1.06
O IV	555.263	5.25	22.54±0.65	22.41	0.99
O IV	608.332	5.25	16.28±2.83	16.56	1.02
O V	629.732	5.35	308.15±4.25	336.72	1.09
Ne V	358.455	5.45	4.35±0.70		
Ne V	569.758	5.45	5.27±0.12	5.09	0.97
Ne V	572.112	5.45	8.21±0.15	8.21	1.00
Ne VI	558.591	5.65	8.44±0.18	7.08	0.84
Mg VII	365.210	5.80	6.13±0.15		
Mg VII	367.675	5.80	14.53±1.51	17.09	1.18
Ca X	557.759	5.80	7.16±0.17	6.20	0.87
Ca X	574.007	5.80	6.18±0.36	3.06	0.50
Mg VIII	313.736	5.90	23.81±1.08	18.81	0.79
Si VIII	314.345	5.90	22.39±1.44	40.53	1.81
Mg VIII	315.024	5.90	59.15±3.70	48.63	0.82
Si VIII	316.220	5.90	41.81±0.92	80.77	1.93
Mg VIII	317.008	5.90	15.61±0.40		
Si VIII	319.839	5.90	49.92±1.44	120.63	2.42
Mg VIII	339.000	5.90	10.44±0.73		
Mg IX	368.063	6.00	220.73±4.41	206.01	0.93
Si IX	341.974	6.05	16.11±0.75	19.32	1.20
Si IX	345.130	6.05	45.71±1.70	45.46	0.99
Fe X	345.735	6.05	28.65±1.62		
Si IX	349.872	6.05	38.24±1.05	39.71	1.04
Fe X	365.565	6.05	12.30±0.97		
Mg X	609.786	6.05	93.87±1.91		
Mg X	624.950	6.05	34.08±0.40	41.07	1.21
Fe XI	341.114	6.10	11.96±0.63	5.93	0.50
Fe XI	352.672	6.10	30.16±1.14	24.82	0.82
Fe XI	369.163	6.10	8.55±0.40	7.46	0.87
Fe XII	346.857	6.15	10.05±0.57		
Si X	347.406	6.15	46.84±1.07	35.76	0.76
Fe XII	352.106	6.15	21.03±0.92	25.37	1.21
Si X	356.027	6.15	27.85±1.23	18.37	0.66
Fe XII	364.468	6.15	31.42±2.74	36.87	1.17
Si XI	303.326	6.20	112.15±14.90	98.25	0.88
Fe XIII	320.800	6.20	8.65±0.85		
Fe XIII	348.182	6.20	10.43±2.07	22.54	2.16
Si XI	580.920	6.20	4.03±0.12		
Fe XIV	334.171	6.25	8.52±0.43	9.19	1.08
Si XII	520.662	6.25	4.73±0.11	4.55	0.96

[a] Units are erg cm^{-2} s^{-1} sr^{-1}.

TABLE 2
COMPARISON OF OBSERVED AND PREDICTED COUNT RATES.

Instrument	λ (Å)	Obs	DEM	DEM[a]	A&R[a]	A&R (N_e)[a]
TRACE	171	1.32	1.34	1.37	1.60	1.48
TRACE	195	0.71	0.99	0.99	0.68	0.97
TRACE	284	0.28	0.06	0.10	0.09	0.09
EIT	171	135.9	101.0	101.0	110.0	102.2
EIT	195	55.7	52.9	53.0	47.8	57.8
EIT	284	2.50	0.97	0.97	0.76	0.75
EIT	304	70.9	3.84	28.5	29.3	29.0

[a] Indicates that a correction factor of 28.3 has been made for the enhanced He II 304 Å emission.

TABLE 3
COMPOSITE RADIATED POWER LOSS FUNCTION FOR CASE DEM1 (SEE TEXT).

$\log T_e(K)$	$\Lambda(T_e)^a$	$\log T_e(K)$	$\Lambda(T_e)^a$
4.0	1.45×10^{-23}	6.1	3.86×10^{-22}
4.1	7.63×10^{-23}	6.2	3.47×10^{-22}
4.2	2.10×10^{-22}	6.3	2.40×10^{-22}
4.3	1.63×10^{-22}	6.4	1.37×10^{-22}
4.4	1.11×10^{-22}	6.5	8.90×10^{-23}
4.5	1.23×10^{-22}	6.6	7.28×10^{-23}
4.6	1.70×10^{-22}	6.7	7.15×10^{-23}
4.7	2.60×10^{-22}	6.8	7.48×10^{-23}
4.8	4.08×10^{-22}	6.9	7.61×10^{-23}
4.9	5.06×10^{-22}	7.0	7.28×10^{-23}
5.0	5.44×10^{-22}	7.1	6.20×10^{-23}
5.1	5.12×10^{-22}	7.2	4.52×10^{-23}
5.2	5.57×10^{-22}	7.3	3.42×10^{-23}
5.3	6.11×10^{-22}	7.4	2.91×10^{-23}
5.4	6.14×10^{-22}	7.5	2.73×10^{-23}
5.5	4.02×10^{-22}	7.6	2.73×10^{-23}
5.6	2.99×10^{-22}	7.7	2.84×10^{-23}
5.7	3.12×10^{-22}	7.8	3.00×10^{-23}
5.8	3.27×10^{-22}	7.9	3.21×10^{-23}
5.9	3.58×10^{-22}	8.0	3.42×10^{-23}
6.0	3.94×10^{-22}		

[a] Units are erg cm^3 s^{-1}.